The Segmented Waveguide Sensor: Principle and Experiments

Joris van Lith, Paul V. Lambeck, Hugo J. W. M. Hoekstra, Rene G. Heideman, and R. R. Wijn

***Abstract*—A novel type of chemooptical sensor has been designed, fabricated, and characterized. The sensor is simple to fabricate, places low demands on light source quality, and shows a resolution of the chemically induced refractive-index changes better than 5.10^{-7}**

***Index Terms*—Guided-wave optics, integrated optics, segmented waveguides, sensing.**

I. Introduction

INTEGRATED OPTICAL (IO) sensor systems have a large potential to be small, very sensitive, and relatively cheap [1]. A novel type of IO sensor based on a segmented waveguide, in which chemically induced changes of refractive index are read out as index-dependent losses, has been investigated. Segmented waveguides have raised a lot of interest due to their potential as devices for quasi-phase matching in second harmonic generation [2] or for tuning the size of the modal field [3], [4], but up until recently they never have been used for sensing purposes.

The segmented waveguide sensor (SWS) has low demands on the technology and on the quality of the light source but still enables high resolution. The sensor can be used as an ON–OFF alarm sensor or for continuous measurements. Using standard peripheral equipment, a resolution of $\delta n = 5.10^{-7}$ is expected to be feasible. In this paper, in Section II, the principle will be treated. Then, in Section III, several methods that can be used to calculate the performances of the SWS will be compared. After that, in Section IV, a theory will be presented that describes the resolution of the total sensor system, consisting of the IO chip and all the peripheral equipment. The design and realization will be presented in Section V. The characterization of the sensor will be treated in Section VI, followed by the discussion and conclusion in Sections VII and VIII, respectively.

II. Device Principle

Chemical IO sensors make use of materials in which the optical properties depend on the concentration of a specific measurand. The IO readout system can then detect a change in refractive index, absorption, or luminescence [1] of this material. Most of the IO sensors that detect a change in refractive index use the dependency of the effective index on the index of the sensing material, and this effective-index change is generally measured using interference effects [5] or mode coupling [6]. The SWS also is a refractive-index-type sensor, but unlike other sensors, it uses the shape of the mode profile to measure the refractive index of the sensing material. It is therefore not necessary, like in other refractive-type sensors (based on interference), to use a narrow-band light source. A sensor that also makes use of the shape of the mode profile has been investigated by Veldhuis [7], [8]: the bend sensor.

An SWS is a waveguide channel that consists of at least two types of segments. In the case of a monomodal waveguide, at each transition between two adjacent segments, power is coupled from the guided mode of one segment into the guided mode of the next segment. The coupling efficiency is determined mainly by the degree of similarity of the mode profiles in both types of segments. The shape of the mode profile in the so-called active segments depends on the refractive index of the sensing material that has been incorporated in the segment. In the other type of segments, this dependency is different or even absent. This dependency is different for both types of segments. This way, the coupling efficiency is a function of the refractive index of the sensing material. The segmentation in the waveguide channel can be realized in various ways. The two types of segments may differ with respect to the cladding material, but also with respect to the core material, or the width of the waveguide channel. In this section the principle will be explained in more detail for a specific type of segmentation: segmentation of the cladding.

In Fig. 1, a longitudinal cross section of the sensing part is depicted: a ridge-type wave-guiding channel consisting alternately of two types of segments: segments with SiON as cladding and segments with a sensing material as cladding. The sensing material is a chemically active material whose refractive index depends on the concentration c of a specific chemical compound. A guided mode is launched into the first segment of the waveguide. We define the difference in refractive index $\Delta n(c) = n_{\mathrm{SiOn}} - n_{\mathrm{sensing}}(c)$, where n_{SiOn} and $n_{\mathrm{sensing}}(c)$ are the refractive indexes of the SiON and sensing material, respectively. If $\Delta n(c) = 0$, all optical power will be transferred to the next segment.

If, however, $\Delta n(c) \neq 0$, then due to the difference in field profiles of both types of segments, not all guided-mode power launched into one segment will be transferred to the guided mode of the adjacent segment. At the transition, radiation will be generated. The amount of power left in the waveguide of course depends on Δn, and hence in the chemooptical sensors we are considering, it is a measure for the concentration of the measurand. If only one transition is used, then the chemically induced change of the loss of guided-mode power Δn generally

Manuscript received October 28, 2003; revised July 19, 2004.

The authors are with the IOMS, MESA$^+$-Institute, University of Twente, 7500 AE Enschede, The Netherlands (e-mail: J.vanLith@el.Utwente.nl).

Digital Object Identifier 10.1109/JLT.2004.834982

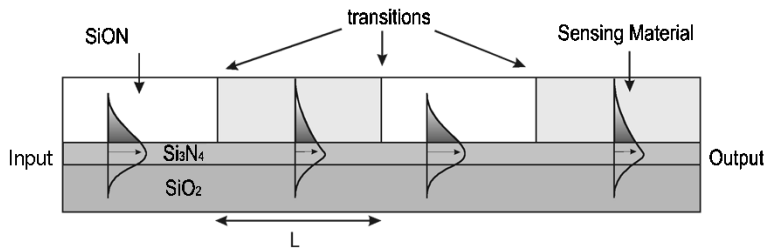

Fig. 1. Longitudinal cross section of the sensor.

is very small; however, with a sequence of a few thousand transitions, a quite sensitive sensor can be obtained.

Part of the power radiated out at one transition will be recaptured into the guided mode at one of the next transitions. It is the distance L between two neighboring transitions that determines both the amount and phase of the field that is coupled back into the guided mode. Depending on the phase difference, there can be constructive or destructive interference between the original guided mode and the radiation coupled back into the guided mode. Although not required, for simplicity reasons, we have chosen here and in the remainder of the paper for a periodic structure. Note, however, that the principle works for any distribution of segment lengths and that the nature of the distribution itself also is a design parameter. Note also that, in the above, we silently assumed that no backward-propagating modes are generated at the transitions, an assumption that is supported by all our calculations. In the regime of indexes used for the sensor, backward scattering is negligibly small. We have also verified that higher order Bragg reflections do not influence the operation of the sensor; for the experimental results depicted in Figs. 6 and 7, the maximum reflection was calculated to be 0.001.

III. Calculation Methods

For a quantitative description of SWS, it is important to have a simulation tool/method available that can handle radiation very well. Unfortunately, we had no three-dimensional (3-D) simulation programs available that could cope accurately with the very thin Si_3N_4 core layers applied in the sensors and could accurately describe the light behavior during its propagations through multiple segments. For this reason, we had to rely on two-dimensional (2-D) methods. Calculations and 3-D simulations, although not very accurate, clearly show that the light coupled into radiation modes at one transition diverges very little in the lateral direction, but considerably in the transversal direction. For short propagation distances, the field distribution in the lateral direction can be well approximated as being constant, and therefore it is a good approximation to replace the 3-D SWS structure with an equivalent 2-D slab structure shown in Fig. 1, now being invariant in the transversal direction.

Three 2-D methods have been used: a finite-difference beam-propagation method (FD-BPM) [11], a bidirectional eigenmode-propagation (BEP) method [11], and a spectral decomposition method (SDM) [12], [1]. Each of these calculation methods has its strong and weak points, and they all have their specific points to which extra attention has to be paid. Application of these methods to the segmented waveguide structure is not trivial.

Calculations [12], simulations, and experimental results show that for this type of SWS, the functional loss η of the guided mode presented in decibels is approximately, for low losses, proportional to the square of Δn around $\Delta n = 0$. As will appear later on in the paper, the SWS will usually operate in a state very close to $\Delta n = 0$.

$$\eta(\Delta n) = A.L_{\text{sensor}}.\Delta n^2. \tag{1}$$

Here, $\eta(\Delta n)$ denotes the functional loss in deceibels, normalized on $\eta(0)$. L_{sensor} is the total length of the sensor, and A (in decibels per meter) is a constant, of which its specific value depends on the optical and geometrical parameters of the SW structure. The value A is a measure for the quality of the sensor. Note that the sensitivity $(\partial\eta(\Delta n)/\partial\Delta n)$ of the sensor is proportional to L_{sensor}.

In order to validate the simulation methods, calculations have been performed on the structure as is given in the "design" section in Fig. 4 and Table I. The results of all three calculation methods appear to agree reasonably well to each other, as can be seen in Fig. 2(a) and (b). In Fig. 2(a), the L dependence of the functional loss for $\Delta n = -0.01$ calculated by the BEP has been compared with that calculated by the FD-BPM. In addition, the A values calculated by the SDM and the BEP correspond very well. Because the SDM is for the considered structure accurate only for $\Delta n < 0.0001$ and the BPM only for $\Delta n > 0.001$, there is no direct comparison between these two methods possible. Note that for $\Delta n = 0.01$, the approximation assumed in (1) is not valid anymore; therefore, the shape of both characteristics in Fig. 2(a) and (b) are slightly different. The BEP appeared to be the most universal method to simulate the sensors, so most of the calculations mentioned in this paper subsequently will be performed using the BEP.

IV. Resolution Analysis

Every sensor application is characterized by its own specific set of requirements to its performance. Because IO sensors are most competitive if high resolution is required, we will focus on this aspect and analyze the resolution prospects of the SWS. Resolution is defined as the smallest change in refractive index that can be measured by the complete sensing system, consisting of the optical chip with the segmented structure and the peripheral equipment: the light source and the optoelectronic detection system. By this definition, we have excluded the influence of the concentration-to-refractive- index transduction properties of the applied chemically active material. In general, high resolution is required over a small range only.

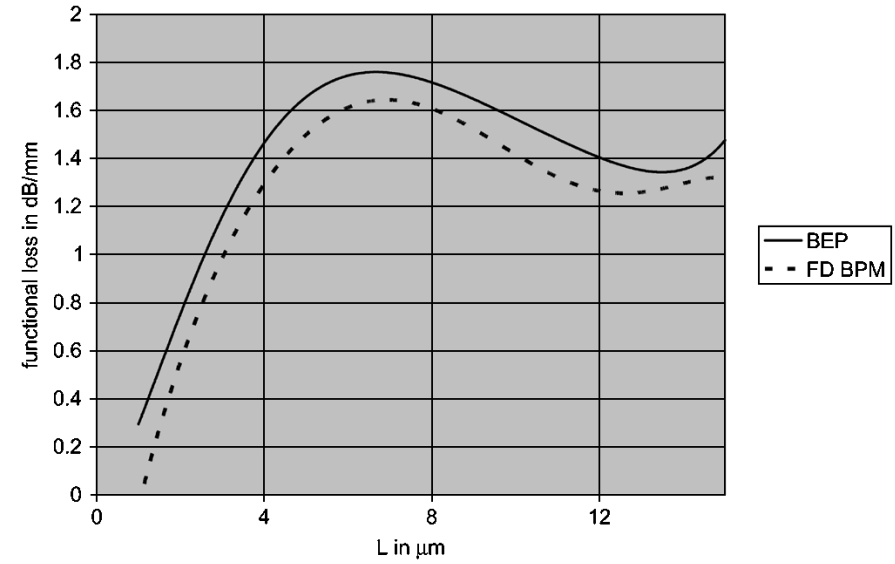

(a)

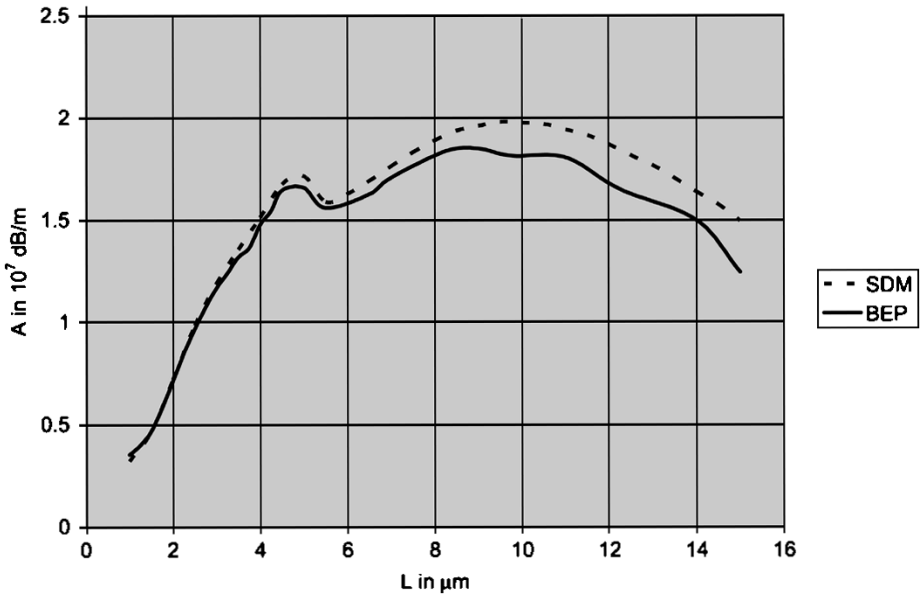

(b)

Fig. 2. (a) Comparison of BEP and FD-BPM for $\Delta n = -0.01$. (b) Comparison of SDM and BEP.

The basic behavior of this sensor can be expressed by the relation

$$P_{\text{out}} = F(\Delta n) P_{\text{in}} \tag{2}$$

where P_{in} and P_{out} are the input and output power of the segmented structure, respectively, and $F(\Delta n)$ represents the transfer function of the sensor. We may assume without loss of generality that in the sensor, which will be analyzed, Δn is positive. Starting from relation (1), $F(\Delta n)$ can be expressed as

$$F(\Delta n) = 10^{-0.1(A\Delta n^2 + B)L_{\text{sens}}} \tag{3}$$

where L_{sens} is the length of the segmented structure. $A\Delta n^2$ is the functional loss as a consequence of the segmentation, and B the propagation loss for $\Delta n = 0$. A is governed by the specific design of the segmented structure, and B is governed mainly by the properties of chosen materials and technology.

The resolution depends on the sensitivity of the sensor S

$$\begin{aligned} S(\Delta n) &= \frac{\partial (P_{\text{out}}/P_{\text{in}})}{\partial n} \\ &= \frac{\partial F(\Delta n)}{\partial n} \\ &= \frac{-\ln(10)}{10} 2A\Delta n F(\Delta n) \end{aligned} \tag{4}$$

and on the accidental errors, i.e., fluctuations, in each of the three quantities given in expression (2). As can be seen from expression (4), the sensitivity is a function of Δn. In practice, the sensor will operate in a very small domain around a fixed Δn, not necessarily $\Delta n = 0$. This Δn will be referred to as the working point, and it will appear to be an important design parameter.

The accidental error in P_{in}, originates from fluctuations in the light source power and the couplings used to transport the light

to the segmented structure. Generally, these fluctuations can be described as a relative error q_1 in the input power and, as a consequence of (2), also as an identical relative error in the output power of the segmented structure. This output power is read out by an optoelectronic system consisting, e.g., of a photodiode and electronic processing units. The accidental error related to this readout system is mostly determined by the photon noise and amplifier noise. We approximate this by an additional relative error in P_{out} denoted by q_2, with its specific value depending on the considered power range. For this approximation to be valid, of course, the output power has to amply exceed the shot noise limit of the photodiode. The influence of temperature fluctuations on the transfer function will be assumed to be effectively suppressed by thermostating the optical chip, while fluctuations in the concentration, and hence in the refractive index of the active layer, will be suppressed by an appropriate way of sample transport to the sensor.

In addition to these accidental errors, systematical errors can exist, e.g., in the transfer function, due to the tolerances of the technological processes for realizing the segmented structure. We shall assume that their effects can be taken into account by calibration.

The resolution δn of the sensor can be calculated from

$$S(\Delta n)\delta n = (q_1 + q_2)P_{\text{out}}/P_{\text{in}}. \tag{5}$$

Inserting expression (2) and (4) in (5) gives us

$$\delta n = \frac{5}{\ln(10)} \frac{(q_1 + q_2)}{A\Delta n L_{\text{sens}}}. \tag{6}$$

In evaluating (6), we have to realize that the advantageous increase of Δn and/or L_{sens} also implies a decrease of P_{out}. Therefore, the lower limit of the dynamic range $P_{\min}$ restricts the allowed Δn–L_{sens}combinations. We can conclude that the best resolution will be obtained if $P_{\text{out}} = P_{\min}$. From this condition, the optimal value of L_{sens} for a given Δn can be calculated to be

$$L_{\max} = \frac{10\log(P_{\text{in}}/P_{\min})}{A\Delta n_{\max}^2 + B} \tag{7}$$

where $\Delta n_{\max}$ is the highest value of Δn that can be measured.

Substituting (7) into (6) gives

$$\delta n = \frac{1}{\ln 10} \frac{q_1 + q_2}{\log(P_{\text{in}}/P_{\min})} \frac{A\Delta n_{\max}^2 + B}{2\Delta n A}. \tag{8}$$

The first factor expresses quantitatively the influence of the peripheral equipment: q_1 and q_2 have to be as small as possible, as could be expected, and the input power as large as possible. The second factor expresses the influence of the segmented structure; its minimum value, as a function of both Δn and $\Delta n_{\max}$, is obtained if $\Delta n = \Delta n_{\max}$ and $\Delta n_{\max} = \sqrt{B/A}$.

Hence, the best resolution that can be obtained is equal to

$$\partial n = \frac{1}{\ln 10} \frac{q_1 + q_2}{\log(P_{\text{in}}/P_{\min})} \sqrt{B/A}. \tag{9}$$

Note that to obtain this resolution, the length of the segmented structures should be

$$L_{\text{sens}} = \frac{10\log(P_{\text{in}}/P_{\min})}{2B}. \tag{10}$$

Expression (8) presents the best resolution, which is obtained at $P_{\text{out}} = P_{\min}$. If a certain minimum threshold concentration of a specific measurand needs to be measured, then the highest resolution is obtained if $\Delta n(c = 0)$ is equal to $\Delta n_{\max}$. Usually, Δn values have to be measured over a certain range. Lower Δn values correspond to higher P_{out} values, and as a consequence they will be measured with worse resolution. Assuming that the lowest Δn value to be measured corresponds with Δn_1, the worst resolution over the given range Δn_1 to $\Delta n_{\max}$ will be

$$\begin{aligned} \partial n_{\text{worst}} &= \frac{1}{\ln 10} \frac{q_1 + q_2}{\log(P_{\text{in}}/P_{\min})} \frac{A\Delta n_{\max}^2 + B}{2\Delta n_1 A} \\ &= \frac{1}{\ln 10} \frac{q_1 + q_2}{\log(P_{\text{in}}/P_{\min})} \frac{B}{A} \frac{1}{\Delta n_1}. \end{aligned} \tag{11}$$

Note, however, that in measuring low concentrations, the Δn changes are generally small; hence, the worst resolution will not differ much from the best one.

Finally, up until now, it was assumed that the refractive index of the cladding layer (n_0) can be controlled with an arbitrarily good accuracy. This is unfortunately not the case, and this will limit the resolution of the sensor system. If the index of the cladding has an inaccuracy of Δn_{acc}, then this can be interpreted as if the Δn is located in an uncertainty domain $[-\Delta n_{\text{acc}} + \Delta n_{\text{acc}}]$. The worst-case resolution is then given by (11) with $\Delta n_1 = \Delta n_{\max} - 2.\Delta n_{\text{acc}}$.

The optimal sensor length, giving the highest resolution, has to be practically realizable. Because straight channels generally are limited to lengths of around 5 cm, longer channels can be realized only by constructing them as spirals. Then, bending losses become a relevant aspect in the design.

V. Design and Realization of the Integrated Optical Structure

An SWS will be designed for demonstrating the correctness of the theory and the feasibility of the technology.

As active material gelatine is chosen, being sensitive for relative humidity (RH) and showing a RH-dependent refractive index in the range 1.50–1.54. This material can be easily spun to layers with thicknesses up to 3 μm, thus enabling the so-called bulk sensing variant. The structure will be realized using SiON technology, enabling well-controlled (tolerance better than 0.001) refractive indexes in the range 1.45 (SiO_2)–2.01 (Si_3N_4). The design has been directed to obtaining optimal resolution, while a simple, and thus low cost, technology is intended. For simplicity, we will consider monomodal waveguides only. The system has been chosen to be operational for a wavelength of 850 nm, because of the availability of inexpensive light sources at that wavelength.

The basic slab structure of the sensor, which will be applied on top of an Si wafer will consist of a thermally oxidized SiO_2

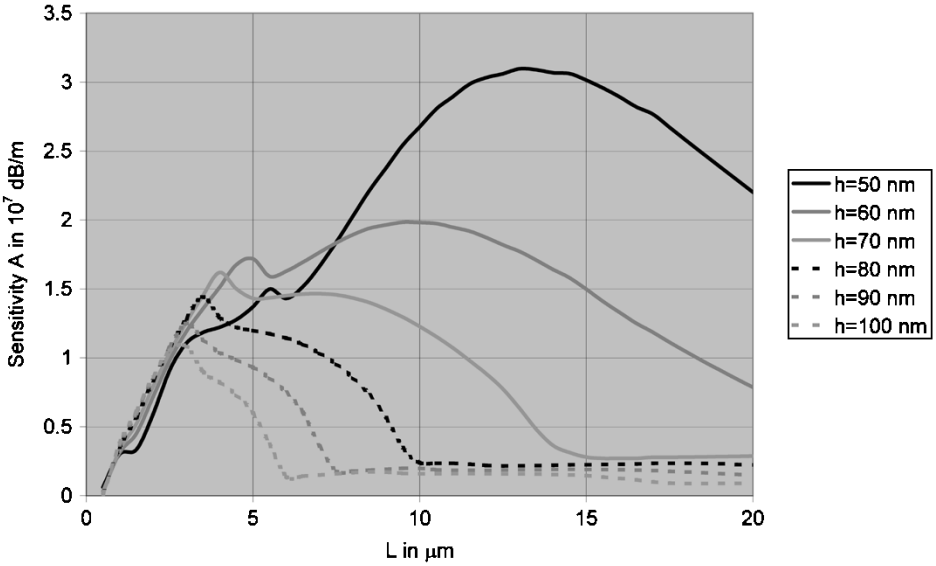

Fig. 3. Comparison sensitivity of SWS with different core thickness.

layer, a low-pressure chemical-vapor deposition (LPCVD)-produced Si_3N_4 core layer (thickness accuracy better than 1%) and a plasma-enhanced chemical-vapor deposition (PECVD) SiON ($n = 1.520$) cladding layer.

The high refractive index of the core layer affords for a high sensitivity of both N_{eff} and the modal-field profile to changes of the refractive index of the cladding material. The fact that the refractive index of the cladding layer is larger than that of the buffer layer enlarges the sensitivity even more [5].

The TE_{00} mode has been launched, because it is possible to design a waveguide in which no TM modes are guided. The thickness of the core layer has to be chosen below 80 nm (cutoff thickness TM_{00} mode) and higher than 44 nm (cutoff thickness TE_{00} mode). A buffer layer thickness of 2.5 μm is sufficient to reduce propagation losses due to leakage of light into the Si wafer to below 0.01 dB/cm for all core layer thicknesses. By limiting the thickness of the entire layer stack to a technologically acceptable (related to layer stress and fabrication time) value of 5 μm, confinement of the modal field within the layer stack asks for a core layer thickness of 60 nm at minimum. Confinement is required to make the passive segments insensitive to changes in the environment and to eliminate scattering caused by the roughness of the upper surface.

The slab height is taken as small as possible (several nanometers) to minimize bend losses. The width of the waveguide is set to 7 μm for optimal fiber-to-chip coupling. This waveguide is multimodal in the lateral direction. However, overlap calculations show that the power coupled to the higher order modes at the fiber-to-chip coupling is negligible. The waveguide channel does not guide TM-polarized modes. Optical connections to this structure have been realized by fibers mounted into V-grooves made in the Si wafer [6]. Lateral alignment is assured because the V-grooves have been defined in the same lithography step as the waveguide channels; transversal alignment is assured by an appropriate width and depth of the V-groove. The output fiber is multimodal in order to collect maximally the output power of the guided mode. For reducing the disturbing effects of slab light generated at the input coupling on the light collection by the output fiber, S-bends have been implemented into the channel before and after the sensing section.

Remaining parameters to be chosen yet are the exact thickness of the core layer and the segmentation. As to the latter, we have simplified the design by choosing identical lengths L for all segments. Segmentation has been realized by reactive ion etching (RIE) of the cladding followed by spinning a 2-μm-thick gelatin layer on top of the IO system.

Using a combination of the EIM and BEP method, we have calculated the A value (a good measure for the sensitivity of the sensor) as a function of the segment length L for various values of the core layer thickness (see Fig. 3).

The curves clearly show that the thinner the core layer, the larger the effects. This can be explained by the larger power fraction in the cladding, which facilitates a larger difference between the field profiles of both types of segments for a given Δn. In addition, the angular distribution of the radiation is a function of the core height. The interplay between the effects of "as many transitions as possible" and "deconstructive interference of radiation modes and guided mode at the transitions" leads to an optimal length being different for different core thicknesses.

Based on the restraints mentioned previously and the simulation results, we have chosen a core layer thickness of 60 nm. The optimum segment length for this core layer thickness is 10 μm. Although from expression (10) and the data given in Table I an optimum length of about 19 cm can be calculated, for easy characterization the L_{sens} has been chosen to be 5 mm. This length is sufficient to give an accurate estimate of the A parameter, to check the validity of the theory, and to demonstrate the feasibility of the technology. The A parameter can be used to make an accurate estimate of the possible resolution that can be achieved with this kind of sensor. To actually demonstrate this high resolution, however, sensors with much larger lengths should be fabricated. This will be the next step in our research.

The layer stack with its optical properties is depicted in Fig. 4; the parameters of the designed structure are listed in Table I.

TABLE I
PARAMETERS OF THE DESIGNED SWS AND PROPERTIES OF THE REALIZED SWS

Parameter	Intended Value	Realized value	Characterization method
Wavelength	850 nm		
Thickness Si_3N_4 core layer	60 nm	58 ± 0.1 nm	ellipsometry
Channel width	7.0 μm	6.9 ± 0.1 μm	SEM
Thickness SiON cladding layer	2.0 μm	2.00 ± 0.02 μm	ellipsometry
Index SiON	1.520	1.520 ± 0.001	ellipsometry
Underetch SiON		0.5 ± 0.1 μm	SEM
Thickness SiO_2 buffer layer	>2.5 μm	2.8 ± 0.1 μm	ellipsometry
Propagation loss (dB)		0.5 ± 0.3 dB/cm	light scattering

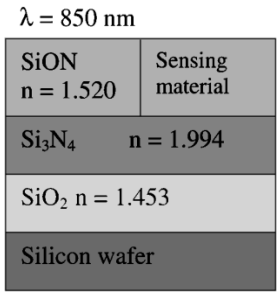

Fig. 4. Layer stack of the SWS.

Using the aforementioned technologies, the structures have been realized. To check the validity of the calculations, structures with different segment length have been fabricated. A scanning electron microscope (SEM) picture of part of a segmented structure is presented in Fig. 5. All relevant structural parameters have been measured either as intermediate steps in the technological process or at the final structure. Results are given in the Table I.

VI. CHARACTERIZATION

Measurements of the output power as a function of the relative humidity showed to be not very producible, and also a large hysteresis had been observed. We attribute this to mechanical effects. While equilibrating with the offered relative humidity, the refractive-index change of the gelatin layer is accompanied by a change of its thickness. Due to the adhesion of the gelatin to the SiON at the transitions at low changes, clamping effects will degrade the intended effects, while at higher changes the materials will be deformed irreversibly. These disturbing effects do not manifest themselves in the flat gelatin layers, which have been applied in evanescent-field-type Mach–Zehnder interferometers. Therefore, we have to conclude that the SWSs are not applicable for such chemooptical transduction layers, in which refractive-index changes are accompanied by considerable swelling.

For testing the SWS now mixtures of liquids have been used, with refractive indexes in the aforementioned range: benzyl–alcohol $(n = 1.54)$ and ethanol $(n = 1.36)$. The index of this mixture was measured with an Abbe refractometer (accuracy $\pm 5.10^{-4}$, white light). They have been fed to the sensor using a flow-through cuvette, which had been clamped on top of the sensing region. Because of the temperature-dependent index and the unknown dispersion, a systematic error of about $\pm 5.10^{-4}$ contributes to the uncertainty in the refractive index. After inserting the liquid in the cuvette, it took about 15 min for the output signal to stabilize; this was probably due to the dead volumes in the cuvette. Substituting the cuvette by a more appropriate microfluidic system in the future may eliminate this problem.

The value of $(q_1 + q_2)$ of the complete sensor system was determined, using direct noise measurements, to be 0.002. P_{in} was about 1 mW and $P_{\min}$ about 1 μW. The output power was measured as a function of Δn. A typical experimental result is shown in Fig. 6, where the functional loss is given for a 1-mm sensor length as a function of Δn.

Because the refractive index of such a mixture could not be determined exactly, the whole characteristic has been shifted along the Δn-axis to put the minimum in functional loss at $\Delta n = 0$. This shift was within the accuracy of the refractive-index measurements. In Fig. 7(a) and (b), both the experimentally obtained and theoretically calculated $\eta(L)$ dependences are presented for $\Delta n = \pm 0.01$. The calculations in this case were performed for the realized structure, which was, due to technological inaccuracies, slightly different from the designed structure. The uncertainties in the value of Δn are the main contribution to the error bars in Figs. 6 and 7. The error in the determination of the functional loss is negligible.

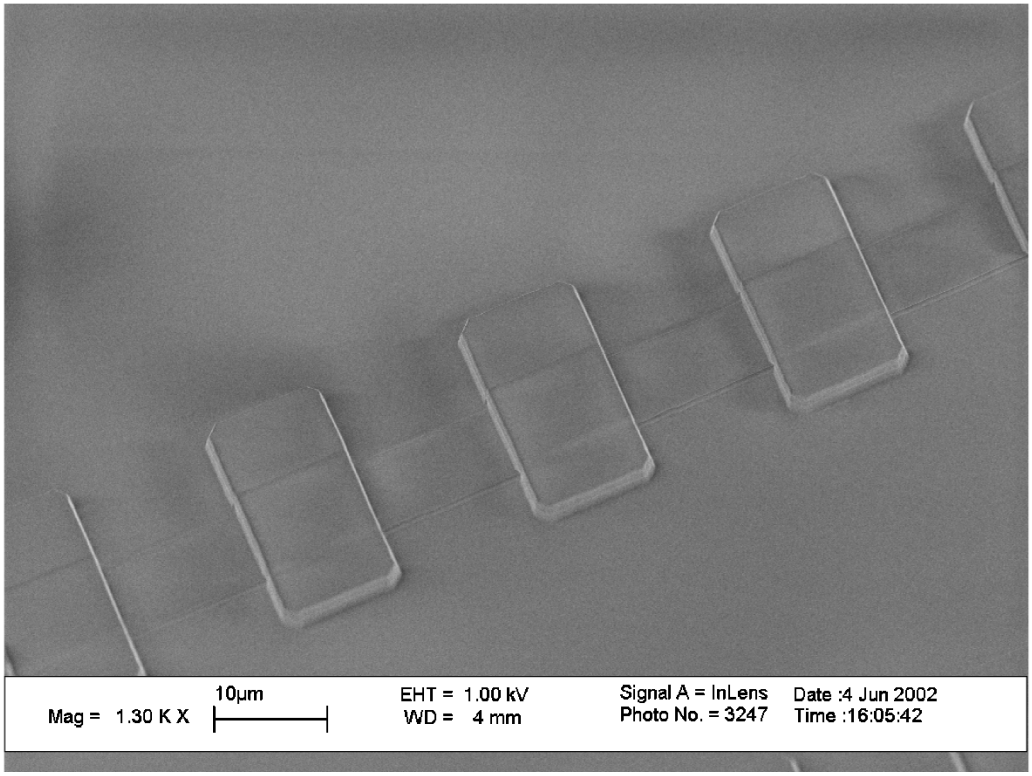

Fig. 5. SEM photo of realized SWS.

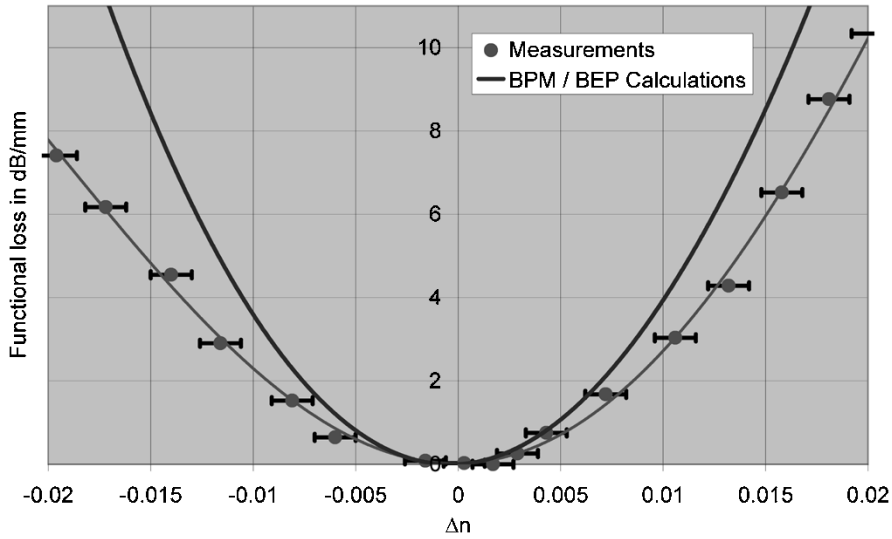

Fig. 6. SWS functional losses for $L = 9$ μ-mm; measurements (points) and simulations (line).

As can be seen, the experimental points agree reasonably well with the theory. We attribute the difference between theory and experiments to the fact that all the calculations were done in 2-D and not in 3-D. The maximum A value of the sensors characterized was 2.7×10^7 dB/m. The B value was about 50 dB/m.

VII. Discussion

The maximum resolution of the realized sensor can be calculated from expression (9) by substitution of the experimentally obtained data. The data refer to the sensing region itself ($A = 2.7 \times 10^7$ dB/m, $B = 50$ dB/m) and the peripheral equipment that was available in our laboratory ($q_1 + q_2 = 0.002, P_{\text{in}} = 1$ mW, and $P_{\min} = 1$ μW). Assuming constant temperature and perfect control of Δn, a resolution $\delta n \approx 5.10^{-7}$ is attainable. A total sensor length $= 25$ cm is required. Using a spiral geometry for the layout of the sensor and only tolerating additional bend losses of less than 0.01 dB/cm, only a 4-mm^2 wafer area is calculated to be necessary for such a sensor. The distance between the adjacent waveguides was taken to be 50 μm to prevent evanescent coupling.

As follows from expression (9), the resolution of the total sensing system is determined by both the properties of the optical sensor and the optical detection system. Lifting some of the

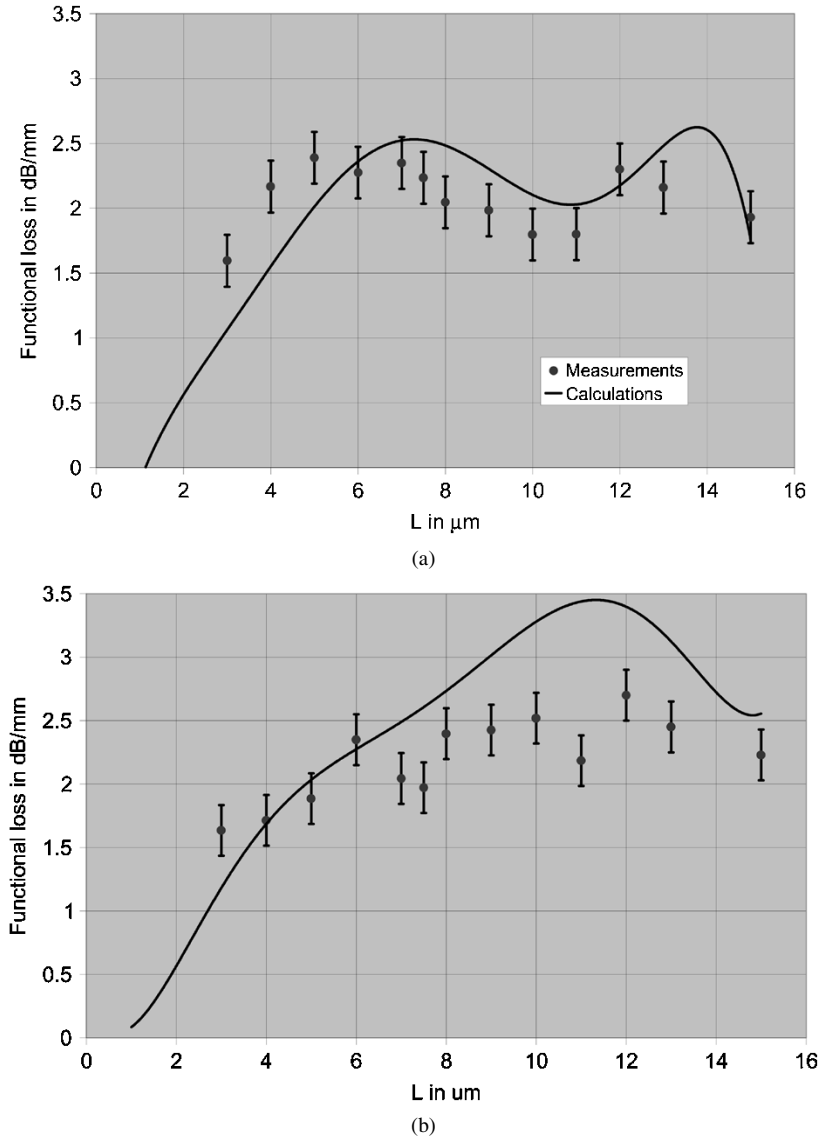

Fig. 7. (a) SWS characteristic $\Delta n = -0.01$. (b) SWS characteristic $\Delta n = +0.01$.

restrictions, we have introduced (identical L, mono-modality) some minor improvement of the resolution is expected only. Major improvement, however, can be achieved by improving the quality of the peripheral equipment. Adding a reference channel can improve the q_1 value. If this reference channel would consist of an identical segmented waveguide as the sensor but with a reference liquid on top, the influence of temperature fluctuations will be strongly reduced. Phase-sensitive detection, of course at the cost of an increase in the price of the peripheral equipment, can reduce noise even further. Based on the specifications of currently commercially available equipment and expected noise reduction using phase-sensitive detection, expected limits of $(q_1 + q_2) = 10^{-4}$ and $P_{\min} = 0.1$ μW will allow for a resolution of $\delta n \approx 2.10^{-8}$.

As stated previously, the segmented waveguide principle can also be implemented in other ways. Two of these are now under investigation and will be explained briefly.

The first one starts from the knowledge that combinations of waveguides with different widths can be designed such that the field profiles of the fundamental mode are very similar [14]. Now, imagine a segmented waveguide sensor with two kinds of segments: segments with a wide waveguide and segments with a small waveguide. Only the top cladding above the waveguide consists of a sensing material. The widths are such that the mode profiles are matched for a specific cladding index. If the index of the sensing material changes, the mode profiles in both kinds of segments change in opposite ways: one mode profile becomes narrower and the other wider. Thus, again the field overlap at transitions between the segments is a function of the refractive index of the top cladding. Notice that the working point n_0, corresponding to minimum loss, is now determined by the combination of waveguide widths.

A second modification we propose is directed to application in immuno-sensing. Here, the sensitive cladding layer can be a mono molecular layer of antibodies (thickness $\sim$4 nm) functioning as receptor sites for specific virus particles (anti-genes). The filling of receptor sites is experienced by the guided mode as an increase of the cladding thickness. For accuracies required for immuno-sensing, this change in average thickness has to be detected very accurately. Let us assume that it is possible to pat-

tern immuno-layers and to use this patterned immuno-layer to define a strip-loaded waveguide channel. Also assume that it is possible to make the immuno-layers locally insensitive so that it is possible to make a segmented waveguide with insensitive and sensitive segments. Because of the very weak lateral confinement of the guided mode in this kind of structure, the width of the modal profile will depend strongly on the height of the ridge. This means that at the interface between the segments, the modal overlap of the guided modes of the two different segments also will depend very strongly on the effective immuno-layer thickness. Note that this kind of SWS makes use of a change of the modal field in lateral direction, while the SWS treated in this paper uses a change in transversal direction.

These modifications will be investigated in more detail in the future.

VIII. Summary and Conclusion

A novel type of a refractive integrated optical chemical sensor, the segmented waveguide sensor, has been introduced. This sensor combines a simple technology with a resolution in the refractive index of the chemooptical transduction layer better than 5.10^{-7}. This sensing principle has been analyzed theoretically, and an expression for the resolution has been derived taking into account properties of both the sensing structure and the peripheral equipment. An SWS has been designed and realized using SiON technology. Experimentally obtained performance corresponds reasonably well with the calculations performed with several 2-D simulation programs. Further optimization of the sensing system is expected to enable improved performance up to a resolution of 2.10^{-8}. Two more implementations of this principle have been suggested.

References

[1] P. V. Lambeck, "Integrated optics for the chemical domain," in *Proc. Eur. Conf. Integrated Optics (ECIO 2001)*, pp. 153–163.

[2] J. Webjorn, F. Laurell, and G. Arvidsson, "Fabrication of periodically domain-inverted channel waveguides in lithium niobate for second harmonic generation," *J. Lightw. Technol.*, vol. LT-7, no. 10, pp. 1597–1600, Oct. 1989.

[3] Z. Weissman and I. Hendel, "Analysis of periodically segmented waveguide mode expanders," *J. Lightw. Technol.*, vol. 13, no. 10, pp. 2053–2081, Oct. 1995.

[4] Z. Weissman, "Evanescent field sensors with periodically segmented waveguides," *Appl. Opt.*, vol. 36, no. 6, pp. 1218–1224, 1997.

[5] O. Parriaux and G. J. Vledhuis, "Normalized analysis for the sensitivity optimization of integrated optical evanescent wave sensors," *J. Lightw. Technol.*, vol. 16, no. 4, pp. 573–582, Apr. 1998.

[6] R. G. Heideman and P. V. Lambeck, "Remote opto-chemical sensing with extreme sensitivity: Design, fabrication and performance of a pigtailed integrated optical phase-modulated Mach–Zehnder interferometer system," *Sens. Actuators B, Chem.*, vol. B61, no. 1–3, pp. 100–127, 1999.

[7] B. J. Luff, R. D. Harris, J. S. Wilkinson, R. Wilson, and D. J. Schriffrin, "Integrated-optical directional coupler biosensor," *Opt. Lett.*, vol. 21, no. 8, pp. 618–620, 1996.

[8] G. J. Veldthuis, L. E. W. van der Veen, and P. V. Lambeck, "Integrated optical refractometer based on waveguide bend loss," *J. Lightw. Technol.*, vol. 17, no. 5, pp. 875–864, May 1999.

[9] G. J. Veldthuis and P. V. Lambeck, "Highly-sensitive passive integrated optical spiral-shaped waveguide refractometer," *Appl. Phys. Lett.*, vol. 71, no. 20, pp. 2895–2897, 1997.

[10] K. Wörhoff, P. V. Lambeck, and A. Driessen, "Design, tolerance analysis, and fabrication of silicon oxynitride based planar optical waveguides for communication devices," *J. Lightwave Technol.*, vol. 17, no. 8, pp. 1401–1407, Aug. 1999.

[11] C2V Software, OlympIOs, Enschede, The Netherlands, version 5.1.12.

[12] S. Gaál, "Novel methods to calculate guided and radiation modes in slab and channel waveguides," Ph.D. dissertation, Integrated optical Microsystems Group, Univ. of Twente, Enschede, The Netherlands, Dec. 2002.

[13] H. J. W. M. Hoekstra, J. van Lith, S. Gaál, and P. V. Lambeck, "The spectral decomposition method: A transparent theory for losses in segmented waveguides," in *Proc. ECIO 2003*, pp. 339–342.

[14] T. Tamir, *Topics in Applied Physics*, 2nd ed. New York: Springer-Verlag, 1979, vol. 7.

Joris van Lith, photograph and biography not available at the time of publication.

Paul V. Lambeck, photograph and biography not available at the time of publication.

Hugo J. W. M. Hoekstra, photograph and biography not available at the time of publication.

Rene G. Heideman, photograph and biography not available at the time of publication.

R. R. Wijn, photograph and biography not available at the time of publication.